Time Reversal Beamforming of Guided Waves in Pipes with a Single Defect

Nicholas O'Donoughue, Joel Harley, José M.F. Moura
Electrical and Computer Engineering, Carnegie Mellon University, Pittsburgh, PA

***Abstract*—Structural health monitoring of buried pipelines is an important application for aging infrastructures. Ultrasonic guided wave inspection is an attractive tool, due to the long propagation of guided waves in the wall of a hollow cylinder. However, guided waves present a unique environment with heavily multi-modal signal propagation and complex dispersion (frequency-dependent propagation speeds). In order to alleviate these challenges, conventional techniques rely on high-voltage excitation with complex transducer arrays, but these systems are not conducive to a monitoring solution. Instead, they require periodic excavation and testing.**

In prior work, we have shown that Time Reversal allows for reliable detection with relatively simple antenna arrays that can be operated in low-power. This paper focuses on localization of these defects. We utilize a beamforming approach that makes use of theoretical dispersion curves to generate fault images. We show through simulations that Time Reversal Beamforming achieves high-resolution localization of a fault in the presence of strong dispersion and heavily multi-modal propagation.

***Index Terms*—Time Reversal, beamforming, dispersion**

I. Introduction

Buried pipelines are an essential piece of any country's infrastructure, as they are used to transport and distribute fuels such as Natural Gas to, and remove waste from, urban centers, businesses and homes. In the case of Natural Gas, an undetected leak represents a catastrophic risk that may lead to loss of life, property, and revenue and potential for explosion. Thus, it is vital to employ structural health monitoring systems to ensure that faults are quickly detected and resolved. Guided waves, which are the hollow cylinder analog to Lamb waves in plates, are often used due to their long propagation and low attenuation. However, guided waves suffer from dispersion (frequency-dependent propagation speeds), which smear signal responses in time. Furthermore, in a given frequency band, there are multiple solutions to the wave equations, resulting in a large number of wave modes. In order to alleviate these challenges, conventional techniques rely on high-voltage excitation with complex transducer arrays to limit wave mode excitation and narrowband signals to limit dispersive effects.

In prior work, we have shown that Time Reversal can be used to detect faults in the dispersive environment created by pipes [1], [2]. The application of Time Reversal allows us to use the effects of dispersion and multi-modal propagation as a constructive source of information, which is contrary to the conventional view of these effects as detrimental. Since we seek to excite strong dispersive effects, we utilize a wideband sinc excitation as opposed to the conventional approach of narrowband signals. Furthermore, since we seek to excite several different wavemodes, we utilize single-transducer excitations, instead of simultaneous probing from complex arrays that are used to selectively excite a single wavemode.

Imaging with Lamb waves has been extensively studied, mostly for imaging in thin plates. Sicard, Chahbaz and Goyette [3] propose a Lamb-wave based Synthetic Aperture Focusing Technique (L-SAFT) algorithm for imaging and detection in the presence of a dispersive wave mode. Rajagopalan, Balasubramaniam and Krishnamurthy [4] consider a beam steering approach. Both of these algorithms are limited to single-mode excitations and are not suitable for the wideband, multi-modal excitations that we consider.

For imaging, we turn to Time Reversal Adaptive Interference Canceling [5] by Jin and Moura, which was developed for RADAR-type applications. They develop a method for imaging via Time Reversal with both Beamforming and MUSIC algorithms. We will concentrate on the Time Reversal Beamforming application in this study, and will modify it for use with guided waves.

Section II outlines the physical model and variables used in this paper. We describe the imaging approach in Section III, discuss the unique aspects of our application in Section IV, and detail simulation results in Section V. Finally, Section VI concludes the paper.

II. Physical Model

We consider the case of a hollow cylinder and utilize cylindrical coordinates (r, θ, z). The cylinder has inner radius r_a and outer radius r_b. The governing wave equations have been solved by Rose [6]. If we consider guided waves propagating in the z-direction, then the solutions are broken into three distinct sets: Longitudinal, Torsional, and Flexural. All three sets of waves exist for an infinite number of modes $m = 1, 2, 3, \ldots, \infty$. Longitudinal waves are axisymmetric waves with displacement in the (r, z) plane, and Torsional waves are axisymmetric waves with displacement in the θ-direction. The property of axisymmetry implies that particle displacement is independent of angular position θ. Flexural wave modes arise from the existence of standing waves in the θ direction, and exist for an infinite number of circumferential orders, $n = 1, 2, 3, \ldots, \infty$. These circumferential orders refer to the number of stationary points in the standing waves. We

National Energy Technology Laboratory (NETL) is the funding source for this effort with Cost Share being provided by Carnegie Mellon University (CMU). Concurrent Technologies Corporation (CTC) is funded under a cooperative agreement with NETL. CMU is funded under a Subcontract Agreement with CTC. Nicholas O'Donoughue and Joel Harley are supported by National Defense Science and Engineering Graduate Fellowship, sponsored by the Army Research Office and the Office of Naval Research, respectively.

adopt the notation in [6] by referring to the Longitudinal and Torsional modes of order m with L(0,m) and T(0,m), respectively, and the n-th circumferential Flexural mode of order m with F(n,m).

If we consider a single wave mode m and circumferential order n, the out-of-plane displacement u of a particle at coordinates (r, θ, z) at time t can be expressed [6]:

$$u_{n,m}(t; r, \theta, z) = \alpha_{n,m}(r) \cos(n\theta) \cos(\omega t + kz), \quad (1)$$

where ω is the frequency of the narrowband excitation signal and k is the angular wavenumber. The amplitude term $\alpha_{n,m}(r)$ is an attenuation factor that is dependent on the wave mode, and varies with depth in the wall of the cylinder. Guided waves in thin plates and cylinders experience a phenomenon known as dispersion, which means that the phase velocity is dependent on the product of the frequency and the thickness of the cylinder wall (called the fd product). Furthermore, each wavemode has a unique dispersion curve. Thus, we express the phase velocity as a function of wave mode m, circumferential order n, and frequency ω for a given cylinder: $c_{p;n,m}(\omega)$. Since we are limiting this study to out-of-plane displacement, the Torsional wave modes will be ignored. The wavenumber k can be expressed as a function of frequency and phase velocity, so we introduce the notation:

$$k_{n,m}(\omega) = \omega / c_{p;n,m}(\omega). \quad (2)$$

We assume that all measurements and excitations are taken on the exterior wall of the pipe, so r is a constant, and we can drop it from our notation.

As stated in the introduction, we are considering wideband excitation signals. We assume that the output is sampled at frequencies ω_q for $q = 0, \ldots, Q-1$. The number of frequency samples Q is chosen such that the samples are separated by the coherence bandwidth of the channel, as decribed in [7]. This allows us to assume that each frequency sample is an independent measurement of the channel.

A. Channel Response

To calculate the guided wave channel response for a given cylinder, we compute the temporal Fourier transform of $u_{n,m}(t; r, \theta, z)$ and take the superposition of all of the wave modes and circumferential orders present. The Fourier transform of a single wave mode is:

$$U_{n,m}(\omega_q; r, \theta, z) = \frac{1}{2} \alpha_{n,m}(r) \cos(n\theta) e^{j k_{n,m}(\omega_q) z}. \quad (3)$$

Thus, the superposition gives us:

$$U(\omega_q; \theta, z) = \frac{1}{2} \sum_{n=0}^{\infty} \sum_{m=0}^{\infty} \alpha_{n,m} \cos(n\theta) e^{j k_{n,m}(\omega_q) z}, \quad (4)$$

where $n = 0$ corresponds to the Longitudinal wave modes and $n \geq 0$ is the set of Flexural wave modes. This equation is the channel response at position (θ, z) for an excitation of frequency ω_q centered at the origin $(\theta_0, z_0) = (0, 0)$. To express the response at some defect location, (θ_d, z_d), from an excitation at (θ, z), we use the short-hand notation:

$$U_d(\omega_q; \theta, z) = U(\omega_q; \theta_d - \theta, z_d - z). \quad (5)$$

B. Response Matrix

We consider two transducer arrays, labeled array A and array B, with P and N transducers, respectively. The two arrays are placed at axial positions z_A and z_B, with the assumption that $z_B > z_A$. The angular positions are given:

$$\boldsymbol{\theta}_A = [\theta_{A_1}, \theta_{A_2}, \ldots, \theta_{A_P}], \quad (6)$$

$$\boldsymbol{\theta}_B = [\theta_{B_1}, \theta_{B_2}, \ldots, \theta_{B_N}]. \quad (7)$$

We define the $N \times P$ clutter channel response matrix, $\mathbf{K}_c(\omega_q)$, such that the (i, j)-th element is the response at antenna B_i to an excitation at antenna A_j. Thus:

$$[\mathbf{K}_c(\omega_q)]_{(i,j)} = k(\omega_q; B_i \leftarrow A_j) \quad (8)$$

$$= U\left(\omega_q; \theta_{B_i} - \theta_{A_j}, z_B - z_A\right) \quad (9)$$

This is the response of the channel when there is no defect. The Defect Channel Response is defined as the response of the channel that is induced by the presence of defect. We utilize a point scattering model, thus we assume that the defect to be imaged is a point source. To compute the target channel response, we can calculate the incident field at the point of the defect, treat the defect as a source transmitting that incident wave field, and compute the resulting incident wave field at our receiver. We label the $N \times P$ Defect Channel Response matrix $\mathbf{K}_d(\omega_q)$, and calculate it with:

$$[\mathbf{K}_d(\omega_q)]_{(i,j)} = \tau_d(\omega_q) \quad U_d\left(\omega_q; \theta_{A_j}, z_A\right) \\ * \quad U_d\left(\omega_q; \theta_{B_i}, z_B\right), \quad (10)$$

where $\tau_d(\omega_q)$ is the complex reflectivity of the point source. For an alternative representation, we stack the channel response at the defect from each of the transmit antennae in A into a vector:

$$\mathbf{g}_A(\omega_q; \theta_d, z_d) = \left[U_d\left(\omega_q; \theta_{A_1}, z_A\right), \ldots, U_d\left(\omega_q; \theta_{A_P}, z_A\right)\right]^T. \quad (11)$$

Similarly, we stack the channel response at each of the receivers in B from an input at the defect position:

$$\mathbf{g}_B(\omega_q; \theta_d, z_d) = \left[U_d\left(\omega_q; \theta_{B_1}, z_B\right), \ldots, U_d\left(\omega_q; \theta_{B_N}, z_B\right)\right]^T. \quad (12)$$

Plugging (11) and (12) into (10) yields a subspace representation of the multistatic response matrix $\mathbf{K}_d$:

$$\mathbf{K}_d(\omega_q) = \tau_d(\omega_q) \mathbf{g}_B(\omega_q; \theta_d, z_d) \mathbf{g}_A^T(\omega_q; \theta_d, z_d). \quad (13)$$

III. Time Reversal Beamforming

We adjust the measurement protocol in [5], [8] and [9], with the data collections broken into four stages:

- Clutter Channel Probing ($\mathbf{A} \rightarrow \mathbf{B}$)
- Defect Channel Monitoring ($\mathbf{B} \rightarrow \mathbf{A}$)
- Time Reversal Target Focusing ($\mathbf{A} \rightarrow \mathbf{B}$)
- Image Formation

The reader is referred to [5] for detailed descriptions and proofs of each step. The assumption in [5] is that the target, or defect, is embedded in a field that is rich with nuisance scattering elements termed clutter. They employ waveform reshaping to suppress the clutter response and enable beamforming. In

this paper, we consider a clean propagating medium, with signal complexities caused instead by multi-modal propagation and dispersion. Since the direction of wave propagation is not affected by the clutter, we do not need to suppress the clutter channel response. Instead, we can remove the known clutter contribution through direction subtraction. The modified algorithm is given below.

1. Clutter Channel Probing ($\mathbf{A} \rightarrow \mathbf{B}$)
In this stage, the channel is probed *a priori* with the signal $S(\omega_q)$ in order to characterize the clutter channel response $\mathbf{K}_c(\omega_q)$. It is assumed that this stage can be repeated several times, such that the results can be averaged to suppress the contribution of additive noise. This response matrix will be utilized in later stages to remove the known clutter response, and allow Time Reversal focusing of only the defect response.

2. Defect Channel Monitoring ($\mathbf{B} \rightarrow \mathbf{A}$)
In this stage, the probing signal $S(\omega_q)$ is sent from array B to array A, in order to monitor the scene for the presence of a defect. The resulting data matrix, after removal of the known clutter contributions and ignoring the noise term, is:

$$\mathbf{Z}(\omega_q) = \mathbf{K}_d^T(\omega_q) S(\omega_q). \tag{14}$$

At this point, the response is either simply a collection of noise terms, or a defect response embedded in noise. However, the multi-modal and dispersive nature of this environment means that the defect response may be smeared, reducing the signal-to-noise ratio. In order to compress the defect response, we apply Time Reversal focusing.

3. Time Reversal Defect Focusing ($\mathbf{A} \rightarrow \mathbf{B}$) In this stage, we Time Reverse and re-transmit the data matrix $\mathbf{Z}^*(\omega_q)$ (one column at a time) from $\mathbf{A}$ and collect the response at $\mathbf{B}$. If we collect the received signals, remove the known clutter contribution, and ignore the noise terms, we have the $N \times N$ data matrix:

$$\mathbf{M}^B(\omega_q) = \mathbf{K}_d(\omega_q) \mathbf{K}_d^H(\omega_q) S^*(\omega_q). \tag{15}$$

The entire process (steps 1 through 4) are repeated, with the roles of arrays A and B are reversed. The result is the $P \times P$ data matrix received at array $\mathbf{A}$:

$$\mathbf{M}^A(\omega_q) = \mathbf{K}_d^T(\omega_q) \mathbf{K}_d^*(\omega_q) S^*(\omega_q). \tag{16}$$

4. Image Formation To generate an image, we utilize beamforming. For each data matrix, we define a transmit and receive steering vector. These vectors are electronically steered to scan different pixels in the desired imaging region. The complex output of the two beamformers is:

$$Y^B(\omega_q;\theta,z) = \mathbf{w}_{rB}^H(\omega_q;\theta,z) \mathbf{M}^B(\omega_q) \mathbf{w}_{tB}(\omega_q;\theta,z) \tag{17}$$
$$Y^A(\omega_q;\theta,z) = \mathbf{w}_{rA}^H(\omega_q;\theta,z) \mathbf{M}^A(\omega_q) \mathbf{s}_{tA}(\omega_q;\theta,z) \tag{18}$$

In order to generate an image, we combine the output of the two beamformers, and sum across every frequency. This is the Time-Reversal Beamforming image.

$$I_{TRBF}(\theta,z) = \sum_{q=0}^{Q-1} \left| Y^A(\omega_q;\theta,z) Y^B(\omega_q;\theta,z) \right|^2. \tag{19}$$

A. Steering Vectors

The optimal steering vectors are given:

$$\mathbf{w}_{rB}(\omega_q;\theta,z) = \frac{\mathbf{g}_B(\omega_q;\theta,z)}{\|\mathbf{g}_B(\omega_q;\theta,z)\|} \tag{20}$$

$$\mathbf{w}_{tB}(\omega_q;\theta,z) = \frac{S(\omega_q)\mathbf{g}_B(\omega_q;\theta,z)}{\|\mathbf{g}_B(\omega_q;\theta,z)\| \, |S(\omega_q)|^2} \tag{21}$$

$$\mathbf{w}_{rA}(\omega_q;\theta,z) = \frac{\mathbf{g}_A(\omega_q;\theta,z)}{\|\mathbf{g}_A(\omega_q;\theta,z)\|} \tag{22}$$

$$\mathbf{w}_{tA}(\omega_q;\theta,z) = \frac{S(\omega_q)\mathbf{g}_A(\omega_q;\theta,z)}{\|\mathbf{g}_A(\omega_q;\theta,z)\| \, |S(\omega_q)|^2}. \tag{23}$$

We run into a problem in constructing the optimal steering vectors, however, since the Green's function requires knowledge of all of the wave-mode weights $\alpha_{n,m}$ and the dispersive wavenumber profiles $k_{n,m}(\omega_q)$. PCDISP is an algorithm written for MATLAB that computes theoretical dispersion curves [10], so we utilize results from that package to compute the wavenumbers. Computation of the relative weights, however, is much more complex, and requires knowledge of many environmental conditions. Therefore, we propose the admittedly sub-optimal approach of assuming that every wave-mode has equal weight: $\alpha_{n,m} = 1$. We will study the effectiveness of this assumption in Section V.

B. Direct Subtraction Beamformer

For comparison, we utilize a Direct Subtraction Beamformer, also defined in [5], that operates on the target channel matrix $\mathbf{K}_d(\omega_q)$. The steering vectors are given:

$$\mathbf{w}_B(\omega_q;\theta,z) = \frac{\mathbf{g}_B(\omega_q;\theta,z)}{\|\mathbf{g}_B(\omega_q;\theta,z)\|} \tag{24}$$

$$\mathbf{w}_A(\omega_q;\theta,z) = \frac{\mathbf{g}_A(\omega_q;\theta,z)}{\|\mathbf{g}_A(\omega_q;\theta,z)\|} \tag{25}$$

The DSBF image is given:

$$I_{DSBF}(\theta,z) = \sum_{q=0}^{Q-1} \left| \frac{\mathbf{g}_B^H(\omega_q;\theta,z) \mathbf{K}_d(\omega_q) \mathbf{g}_A^*(\omega_q;\theta,z)}{\|\mathbf{g}_B(\omega_q;\theta,z)\| \, \|\mathbf{g}_A(\omega_q;\theta,z)\|} \right|^2. \tag{26}$$

IV. Discussion

In typical beamforming, the steering vectors consist of delay terms used to select a desired bearing for signal transmission or receipt:

$$\mathbf{w}(\omega_q) = \left[1, \; e^{-\jmath\phi_1\omega_q}, \ldots, e^{-\jmath\phi_{N-1}\omega_q}\right]^T. \tag{27}$$

This arises from the far-field assumption that propagating waves become planar waves and gives rise to the idea of "steering" a beam. As a result of this, the output of a beamformer is typically highly resolved in bearing, but poorly resolved in range. For this reason, images are generated by beamforming with two different arrays. The arrays are often chosen such that each of their respective bearings to the region of interest are vastly different, in order to maximize resolvability in both range and azimuth.

In a pipe, however, guided waves do not follow free-space propagation. In Longitudinal and Torsional waves, for instance, the incident field on the receiving array is independent of the target's angular position. Thus, the idea of "steering" a beam is meaningless in this application. Instead, it is necessary to note that the effects of dispersion are highly range dependent. When waves at two frequencies travel with different propagation speeds, the difference in their Time of Arrival increases as the propagation distance grows. Thus, dispersion carries with it information about the range of the target. Flexural waves have a predictable profile across the array and allow determination of the target's angular position. Thus, we no longer seek to place our arrays in order to maximize difference in their bearings to the region of interest and can simply utilize parallel arrays at different range positions. *Beamforming* in this sense may be more appropriately termed *Spatial Filtering*; however, we continue to use the term *Beamforming* for this imaging approach, owing to its similar implementation (with transmit and receive subspace filters).

V. Simulation Results

In order to verify these results, we conduct a MATLAB simulation. Analytical dispersion curves are computed with PCDISP for a hollow cylinder with inner radius $r_a = .102m$ and outer radius $r_b = .11m$ over the frequency band $f = 0 - 200kHz$, with $Q = 201$ frequency samples. The clutter response is taken to be the free space propagation between arrays A and B, characterized by (8), and the target response is characterized by (13). The arrays are placed at axial positions $z_A = 0.1m$ and $z_B = 6.9m$, with target at $z_d = 2m$. The two arrays are equally sized with $N = P = 8$ transducers spaced uniformly around the pipe, at $\pi/4$ intervals, with the arrays both centered at $\theta = 0$. The target is placed at $\theta_d = 0$, and has uniform reflectivity: $\tau_d(\omega_q) = 1$.

Since a reliable tool does not exist to estimate the relative wave-mode weights $\alpha_{n,m}$, we simulate these by generating a set of exponential random variables. We will conduct two experiments. In the first, the exact weight of each wave mode is available to the beamformer, and can be used to construct the steering vectors, this is the ideal case. In the second, which we refer to as non-ideal, the weights are unknown and are assumed to all equal 1, as was discussed in Section III-A.

We insert additive zero-mean white Gaussian noise with variance σ_n^2. The signal-to-noise ratio is computed:

$$SNR_{dB} = 10\log_{10}\left(\frac{\sum_{q=1}^{Q}\|\mathbf{K}_d(\omega_q)\|_F^2\,|S(\omega_q)|^2}{\sigma_n^2}\right), \quad (28)$$

where $\|\cdot\|_F$ is the Frobenius norm. For these results, SNR = -2dB. For performance analysis, we will consider the 3-dB range resolution and the Integrated Sidelobe Ratio (ISLR). ISLR is computed as the ratio of total energy in the sidelobes to total energy in the mainlobe. For both metrics, smaller values indicate better performance.

Figure 1 shows the results for the ideal case, while figure 2 shows the results for the non-ideal case. The Direct

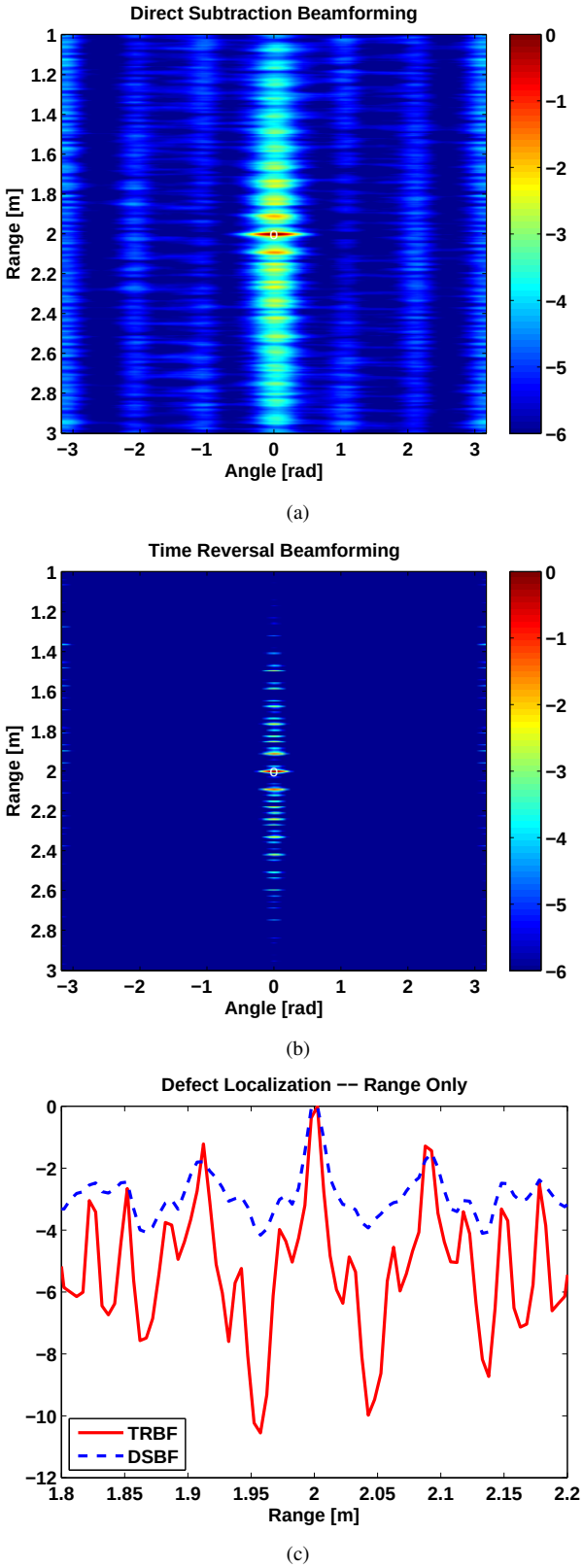

Fig. 1. Imaging results when the wavemode weights are all known. (a) Image generated with Direct Subtraction Beamformer (DSBF). (b) Image generated with Time Reversal Beamformer (TRBF). (c) Range slice (maximum across θ for each z) comparing DSBF to TRBF, showing $z = 1.8, \ldots, 2.2$m.

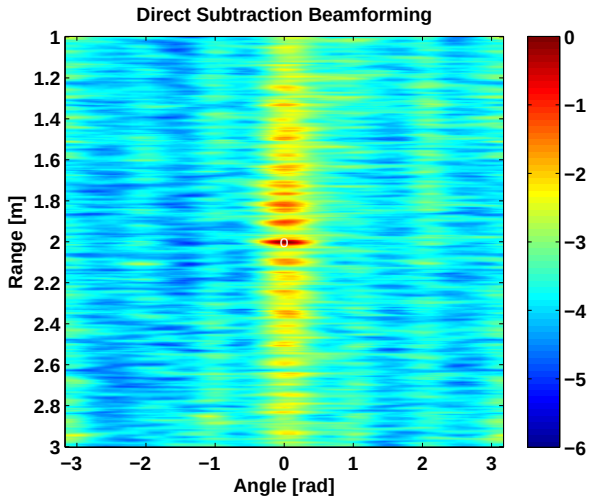

(a)

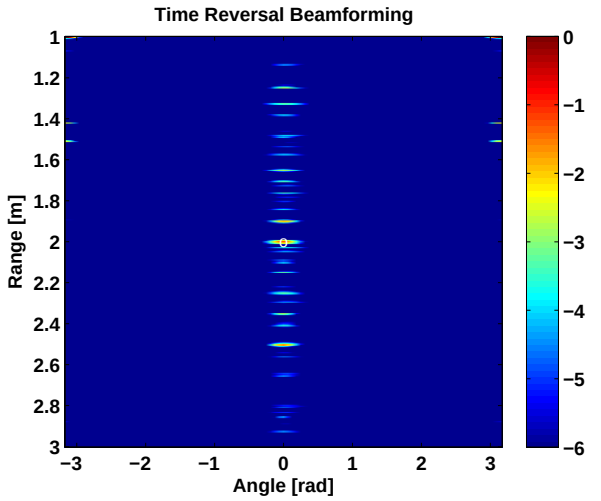

(b)

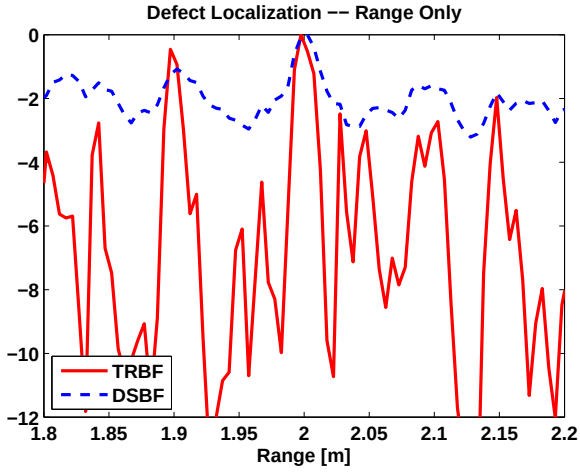

(c)

Fig. 2. Imaging results when the wavemode weights are unknown, and are assumed equal. (a) Image generated with Direct Subtraction Beamformer (DSBF). (b) Image generated with Time Reversal Beamformer (TRBF). (c) Range slice (maximum across θ for each z) comparing DSBF to TRBF, showing $z = 1.8, \ldots, 2.2$m.

Subtraction Beamformer (DSBF) performs well in the ideal case, with a focused target response, but suffers a severe loss of performance in the non-ideal (unknown weights) scenario. The range resolution degrades from 3.6cm in the ideal case to 7.6cm in the non-ideal, a loss of 4cm of resolution. The ISLR increases from 18.05 in the ideal case to 22.27 in the non-ideal case, an increase of 23.4%.

The Time Reversal Beamformer (TRBF) outperforms the DSBF in both scenarios, with a tightly focused peak, and is robust to unknown wave-mode weights. The TRBF achieves a range resolution of 1.6cm in the ideal scenario and 2cm in the non-ideal scenarios, a loss of .4cm resolution. The ISLR increases from 9.4 to 10.16, an 8.1% increase. In both cases, the TRBF loses performance when moving from the ideal to the non-ideal case, as expected, but these performance losses are not as severe as those for the DSBF.

VI. Conclusion

We have derived a beamforming approach to image formation in hollow cylinders, in the presence of heavily dispersive and highly multi-modal signal propagation. We have derived a Direct Subtraction Beamformer to generate a reliable image when all of the channel parameters are known, and a Time Reversal Beamformer that demonstrates robustness to unknown wave-mode amplitudes. Future work will apply these algorithms to datasets from both finite element simulators and laboratory experiments.

References

[1] N. O'Donoughue, J. Harley, J. M. F. Moura, and Y. Jin, "Detection of structural defects in pipes using Time Reversal of guided waves," in *Proc. 43rd Annual Asilomar Conf. on Signals, Systems, and Computers (Asilomar '09)*, Asilomar, CA, November 2009, pp. 1683–1686.

[2] J. Harley, N. O'Donoughue, Y. Jin, and J. M. F. Moura, "Time Reversal focusing for pipeline structural health monitoring," *Proceedings of Meetings on Acoustics*, vol. 8, January 2010.

[3] R. Sicard, A. Chahbaz, and J. Goyette, "Guided Lamb Waves and L-SAFT processing technique for enhanced detection and imaging of corrosion defects in plates with small depth-to-wavelength ratio," *IEEE Trans. on Ultrasonics, Ferroelectrics, and Frequency Control*, vol. 51, no. 10, pp. 1287–1297, October 2004.

[4] J. Rajagopalan, K. Balasubramaniam, and C. V. Krishnamurthy, "A phase reconstruction algorithm for Lamb wave based structural health monitoring of anisotropic multilayered composite plates," *J. Acoust. Soc. Am.*, vol. 119, no. 2, pp. 872–878, February 2006.

[5] Y. Jin and J. M. F. Moura, "Time Reversal imaging by adaptive interference canceling," *IEEE Trans. on Signal Processing*, vol. 56, no. 1, pp. 233–247, January 2008.

[6] J. L. Rose, *Ultrasonic Waves in Solid Media*. Cambridge University Press, 1999.

[7] Y. Jin, J. M. F. Moura, and N. O'Donoughue, "Time Reversal transmission in Multi-Input Multi-Output Radar," *IEEE Journal of Selected Topics in Signal Processing*, vol. 4, no. 1, pp. 210–225, February 2010.

[8] J. M. F. Moura and Y. Jin, "Detection by Time Reversal: Single antenna," *IEEE Trans. on Signal Processing*, vol. 55, no. 1, pp. 187–201, January 2007.

[9] Y. Jin and J. M. F. Moura, "Time-Reversal detection using antenna arrays," *IEEE Trans. on Signal Processing*, vol. 57, no. 4, pp. 1396–1414, April 2009.

[10] F. Seco, J. M. Martín, A. Jiménez, J. L. Pons, L. Calderón, and R. Ceres, "PCDISP: A tool for the simulation of wave propagation in cylindrical waveguides," in *Proc. 9th Int'l Congress on Sound and Vibration*, July 2002, pp. 23–29.